Fachtagung "Lasermethoden in der Strömungsmesstechnik"
3. – 5. September 2013, München

Methoden für die Auswahl der Glättungsparameter und Anwendung von Randbedingungen für Optischen Fluss PIV

Methods for Selecting the Smoothing Parameter and Applying Boundary Conditions for Optical Flow PIV

M. Stark[*], **R. Kapulla**[*], **J. Fokken**[**]
[*] Thermal-Hydraulics Laboratory, Nuclear Energy and Safety Department,
Paul Scherrer Institut, 5232 Villigen PSI, Switzerland
[**] Axpo Power AG, Reactor and Safety Department,
Nuclear Power Plant Beznau, 5312 Döttingen, Switzerland

Schlagworte: PIV, optischer Fluss, Glättungsparameter, datengestützte Randbedingungen
Key words: PIV, optical flow, smoothing parameter, data-driven boundary conditions

Abstract

Using optical flow to analyze particle image velocimetry (PIV) images is a promising technique to increase the resolution of the calculated velocity fields while enabling the analysis of images beyond the capability of traditional cross-correlation algorithms. Based on the conservation of pixel intensity between PIV image pairs, the optical flow algorithm used in this work is a multi-scale adaptation of Horn and Schunck's optical flow. To better adapt the method to the analysis of experimental PIV images, two techniques are proposed; i) an objective framework to aid in selecting the smoothing parameter, and ii) a method to apply physically motivated boundary conditions to the calculated velocity field. Combining both methods in an analysis of an experimental image series with high refractive distortion demonstrates their effectiveness, and further establishes optical flow as a valuable PIV analysis tool.

Introduction

Particle Image Velocimetry (PIV) is a method to extract velocity fields from experimental fluid flows. Traditionally calculated by subdividing the input image pair into "interrogation windows" and using cross-correlation to calculate the displacement of seeding particles between images, the technique is quite robust in analyzing complex flows. However, as detailed by Ruhnau et al., 2005, the use of interrogation windows has some drawbacks:

1. The interrogation window size limits the resolution of the output field. Smaller interrogation windows result in lower correlation peaks, and thus more erroneous vectors, but higher resolution velocity fields.
2. Bulk particle motion within each interrogation window is considered homogeneous, which is not physically true.
3. Velocity estimation does not take advantage of flow structures at different scales, which could be used to infer motion in regions without reliable estimations.

To overcome these limitations, researchers have been investigating other algorithms to supplement or replace traditional cross-correlation methods. One of the most promising is optical flow (Horn & Schunck, 1981), developed by the computer science community for machine-vision. The algorithm works on the premise that for two, 2D projections of a 3D scene (i.e. video frames) there exists

a two-dimensional velocity field which moves the first image toward the second. Beginning with Quénot et al., 1998 and Ruhnau et al., 2005, this analogy was applied to PIV images, which is a physical manifestation of optical flow, where 2D images of illuminated seeding particles are taken of a fluid in which a flow field advects the first image toward the second.

Although optical flow has enjoyed early success in experimental fluid dynamics, some open issues remain. Foremost among them is a suitable way to select the scalar smoothness parameter, used in the variational minimization to balance the data term with the regularizer. Secondly, when analyzing channel flow, both Ruhnau, 2006 and Kapulla et al., 2011 have shown the algorithm's difficulty in resolving boundary layers where the calculated velocity fields exhibit errors near the channel walls where the velocities do not approach zero as expected. In this paper, we propose techniques to overcome both of these issues, and present the results when these techniques are applied to experimental PIV images.

Theory

The optical flow algorithm used throughout this work is based on that of Ruhnau et al., 2005. Their work incorporates the original method of Horn & Schunck in a pyramidal coarse-to-fine motion estimation which is more robust in calculating the large displacements that may be present in PIV image pairs. The method is based on the conservation of image brightness, $I\left(x,y,t\right)$, defined at coordinates x, y for time t, in Equation 1.

$$\frac{DI\left(x,y,t\right)}{Dt} = 0 \tag{1}$$

When differentiated with the chain rule, and using shorthand notation, the brightness consistency constraint of Equation 2 is obtained. I variables are image derivatives along the indicated dimension, while u and v are the x and y components of the velocity field.

$$I_x u + I_y v + I_t = 0 \tag{2}$$

Having only one equation in two variables (u and v), a second condition is needed. In the case of Horn & Schunck, the L2 norm of the velocity gradients, Equation 3, is used.

$$|\nabla u|^2 + |\nabla v|^2 = 0 \tag{3}$$

It is not possible to directly solve Equation 2 and Equation 3 however, since neither is exactly zero due to quantization errors and image noise. Therefore, they are equated to error terms in Equation 4, and combined into a minimization expression together with a scalar weighting parameter α in Equation 5.

$$\mathcal{E}_{dat} = I_x u + I_y v + I_t \tag{4a}$$

$$\mathcal{E}_{reg}^2 = |\nabla u|^2 + |\nabla v|^2 \tag{4b}$$

$$L = \int_\Omega \left[\mathcal{E}_{dat}^2 + \alpha^2 \mathcal{E}_{reg}^2\right] dx\, dy \tag{5}$$

Using the calculus of variations, the minimization of Equation 5 results in the coupled system of Equations 6a and 6b.

$$I_x^2 u + I_x I_y v = \alpha^2 \Delta u - I_x I_t \tag{6a}$$

$$I_x I_y u + \quad I_y^2 v = \alpha^2 \Delta v - I_y I_t \tag{6b}$$

To use Equation 6 in a pyramidal scheme, Ruhnau et al. propose Equation 7, where the Laplacian is split into two components, one using the estimated velocities the current pyramid level, L, and one using the the previous, coarser velocity estimate, $L+1$.

$$I_x^2 u_L + I_x I_y v_L = \alpha^2(\Delta u_L + \Delta u_{L+1}) - I_x I_t \tag{7a}$$

$$I_x I_y u_L + \quad I_y^2 v_L = \alpha^2(\Delta v_L + \Delta v_{L+1}) - I_y I_t \tag{7b}$$

To generate the images needed for the coarse-to-fine motion estimation, a gaussian pyramid is constructed by successively filtering and sub-sampling an input image as shown in Figure 1. To prevent aliasing between levels, additional "scale levels" are generated by further filtering the images at each pyramid level. Velocity field calculation begins on the uppermost pyramid level, on the image with the most filtering, and ends with the original input image pair as shown in Figure 2.

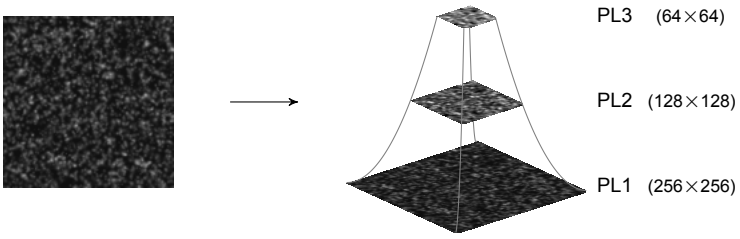

Figure 1: The gaussian pyramid, built from original image (pyramid base) through successive filtering and sub-sampling. Adapted from Ruhnau et al., 2005.

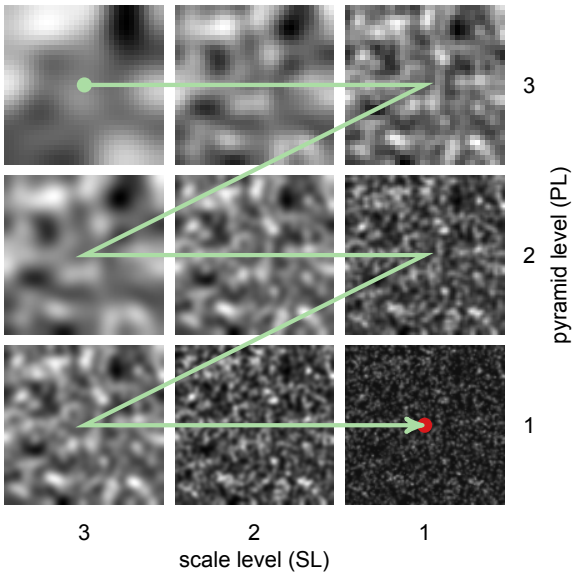

Figure 2: Processing order of the image pyramid together with scale levels. Calculation begins on the most blurred, and down-sampled level (PL3, SL3) and proceeds until the original input image (PL1, SL1).

Smoothing Parameter Selection

Most literature on optical flow present results where the smoothing parameter α in Equations 5 to 7 is heuristically chosen. This is not ideal for fluid flow analysis since an incorrectly chosen value can bias velocity estimates – too large a value results in an overly smoothed velocity field, while too small a value results in a velocity field dominated by noise from the system becoming under-determined (Atcheson et al., 2009). Thus, it is desirable to find a deterministic way to choose the smoothing parameter, with the hope of accurately capturing the underlying flow field of the PIV images.

From the existing literature, only a handful of publications exist which propose an objective way to select the smoothing parameter, the methods of which are summarized below:

- Ng & Solo, 1997: the optimal smoothing parameter minimizes a proposed “risk” function.
- Krajsek & Mester, 2007: the optimal smoothing parameter is selected via a proposed Bayesian framework.
- Zimmer et al., 2011: the optimal smoothing parameter predicts the next image in the sequence most accurately.
- Tu et al., 2012: the optimal smoothing parameter minimizes the difference between warped frames.

Stemming from its ability to predict an optimal smoothing parameter without a priori knowledge of the image noise, its simple framework, and its use of just two image frames, we propose a framework to determine the optimized smoothing parameter for a set of PIV images based on the work of Tu et al., 2012. The idea behind the approach is intuitive; velocity fields calculated with different smoothing parameters are used to warp (i.e. advect) the input images toward each other. The warped image pair with the lowest intensity RMS, calculated using Equation 8, is considered optimally smooth. $I_{w1}(i,j)$ and $I_{w2}(i,j)$ are the per-pixel intensities of the warped images at pixels i and j, with m and n the vertical and horizontal resolution of the images, respectively.

$$\text{Warp RMS} = \sqrt{\frac{\sum_{i=1}^{m}\sum_{j=1}^{n}\left(I_{w1}(i,j) - I_{w2}(i,j)\right)^2}{mn}} \tag{8}$$

The process proceeds as follows:

1. From a single PIV image pair, calculate velocity fields for the series of smoothing parameter values. It is recommended to use values spaced along logarithmic decades, spanning a large range as the error is not necessarily convex and may have local minima.
2. Find the parameter value which results in the lowest warp RMS.
3. Process the entire PIV image series using the chosen smoothing parameter value.

The process is demonstrated using a series of 20 synthetically generated image pairs of pouseuille flow[1], using 5 pyramid levels, and 6 scale levels. Smoothing values are distributed along the logarithmic decades from 0.001–100, and only the first image pair in the series is processed. The warp RMS calculated at each smoothness value is plotted in Figure 3.

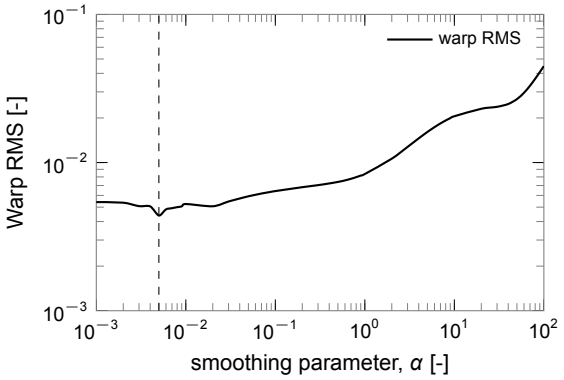

Figure 3: Warp RMS evolution for frames 1 and 2 of the poiseuille image set at various smoothing values.

From Figure 3, the optimal smoothing parameter value is observed around 0.005 and the 19 remaining image pairs are processed with this value. The resulting series averaged velocities are shown along with the ground truth velocities in Figure 4.

[1]Generated by Carlier, 2005. Available at http://fluid.irisa.fr/data-eng.htm

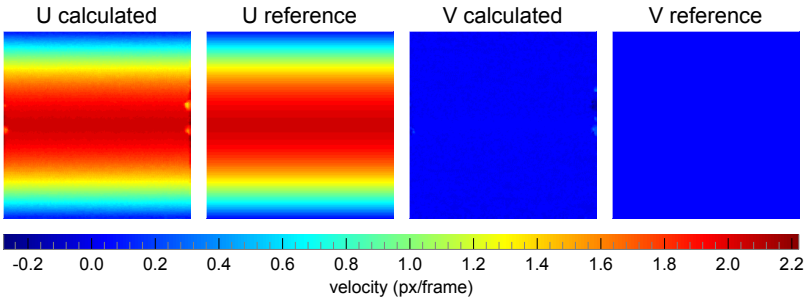

Figure 4: Series-averaged velocity components of poiseuille flow compared to the ground truth velocity field.

Aside from errors on the left and right hand side of the velocity field, where particles enter and leave the image, the calculated velocity field corresponds closely to the ground truth. For a quantitative comparison, series averaged results at each smoothing parameter value are compared to the ground truth using the magnitude error (Equation 9, the L1 norm from Ruhnau et al., 2005) and endpoint error (Equation 10, from Baker et al., 2011). The resulting error curves over the range of smoothing parameters are presented in Figure 5.

$$\text{ME} = \left| \sqrt{u_{calc}^2 + v_{calc}^2} - \sqrt{u_{ref}^2 + v_{ref}^2} \right| \tag{9}$$

$$\text{EE} = \sqrt{(u_{calc} - u_{ref})^2 + (v_{calc} - v_{ref})^2} \tag{10}$$

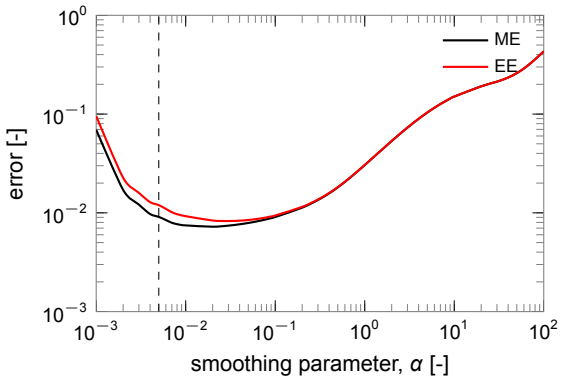

Figure 5: Error evolution of the poiseuille image set at various α values.

Although the proposed smoothing parameter selection underestimates the optimal value from the perspective of minimum average endpoint or magnitude error, the results are nonetheless very good. Considering the average displacement between frames is 1.33 pixels, and the errors at the selected smoothing parameter on the order of 0.01 pixels, the error is less than 1%. This corroborates the qualitative conclusion drawn from Figure 4 that the velocity field calculated with the objectively chosen smoothing parameter adequately captures the underlying flow field of the input images.

Applying Boundary Conditions

By refining a technique of Ruhnau, 2006 where features are added to the input PIV image pairs, we propose a method to reduce velocity errors in boundary regions. Example patterns to be added to the side of the image where the boundary condition is enforced are given in Figures 6 and 7 for no-slip, and parallel conditions, respectively. The patterns are oriented so the boundary condition is applied along the lower edge, and have intentionally been kept small to not significantly increase processing time.

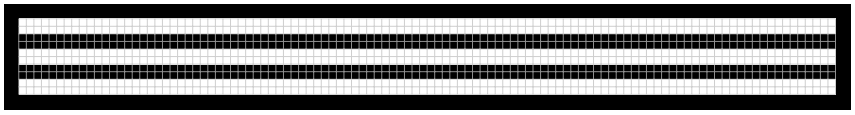

Figure 6: Parallel boundary condition shown on a pixel grid.

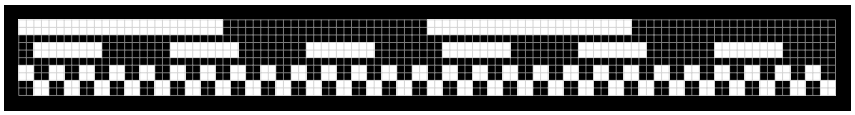

Figure 7: No-slip boundary condition shown on a pixel grid. The pattern is unique over 108 pixels, being designed to handle images with large displacements.

By adding the same patterns at the same location in both input images, motion can be constrained along intensity iso-gradient lines. By modifying the pattern, one can change type of the intended boundary condition; pattern variations in the y-direction constrain motion in the y-direction, while pattern variations in both directions constrain motion in both directions. And, since the condition is only enforced where an intensity gradient exists, one can change strength of the boundary condition, many small alternating features impose a distributed, albeit slightly weaker boundary condition compared to a few large alternating features imposing a stronger condition at fewer points.

Since the technique only requires the addition of the patterns to the input images, only the data term of Equation 5 is affected, making the boundary conditions “data-driven”. Consequently, it can be used with existing optical flow codes without requiring any modification. It should be pointed out that although the proposed patterns have been found to be very effective, care must be taken with analysis using very large smoothing values, which can override the desired effect of the data-driven boundary conditions.

To demonstrate the effect of the proposed boundary conditions on the calculation of velocity fields, results obtained from a single pair in the poiseuille image set are presented with the previously determined smoothing parameter value of 0.005. Consistent with the ground truth (reference) velocity field, a no-slip boundary condition is used, and compared to the same velocity calculation without the patterns added (no b.c.) in Figure 8.

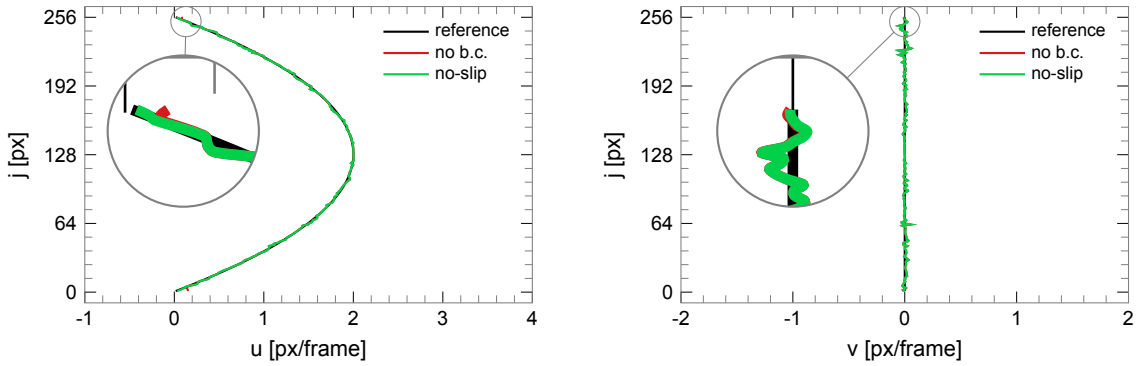

Figure 8: Velocity profile of the poiseuille flow with and without the no-slip boundary condition. u velocity profile on the left, v on the right.

Additionally, the GEM_12 results of Kapulla et al., 2011 have been reprocessed with the use of data-driven boundary conditions. The synthetic images, which were generated from a large eddy simulation (LES) of density mixing in a channel, have been analyzed using a smoothing value of 0.09 as reported in the original study. Velocity profiles extracted at i = 200px are shown in Figure 9.

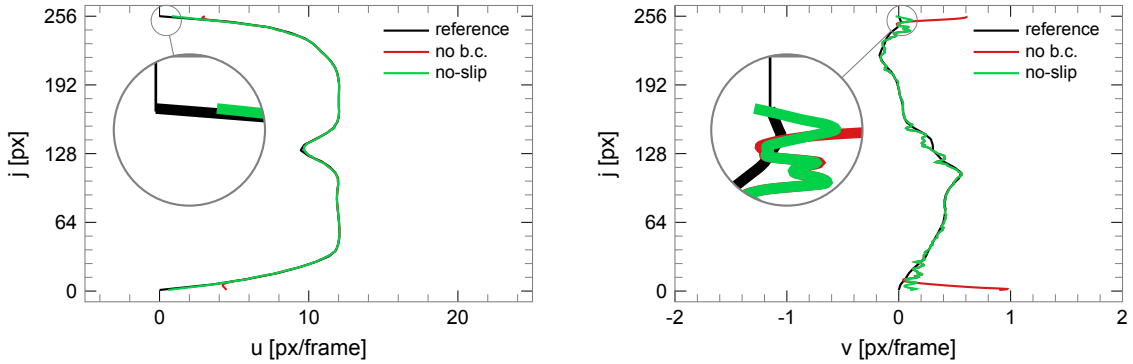

Figure 9: Velocity profiles of the GEM_12 flow with and without the no-slip boundary condition. u velocity profile on the left, v on the right, see Kapulla et al., 2011.

Although in both cases, the u velocity component does not reach *exactly* zero at the wall, the profiles in the boundary regions have been improved considerably. For both the poiseuille and GEM velocity fields, the correct velocity profiles were extracted without lowering the smoothing parameter, implying that the velocities are not over-smoothed in this high-gradient region by a sub-optimal smoothing value, as previously suggested by Kapulla et al., 2011.

Experimental Results

Combining the concepts of smoothing parameter selection and data-driven boundary conditions, a series of experimental PIV images are analyzed. Images are taken from a GEneric MIXing (GEMIX, see Eggertson et al., 2011) density mixing experiment, where two inlet streams, de-ionized water above, and sugar-water solution below, mix in a square channel as shown in Figure 10. The 10% density difference between the two inlet streams causes refractive distortion which blurs the particle images in the mixing region, and parts of the laser light sheet are reflected into the camera. The experimental images are well suited to optical flow over traditional cross-correlation analysis since correlation strength is particularly weak in the blurred mixing zone, the region of interest, .

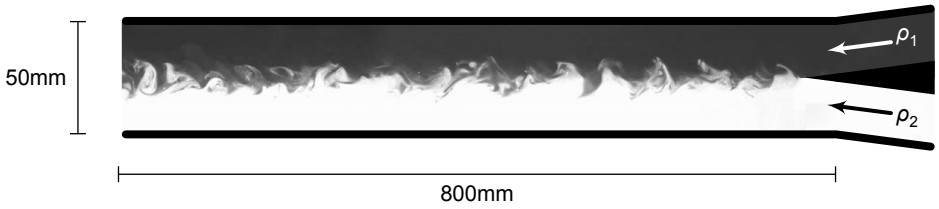

Figure 10: Schematic of the GEneric MIXing (GEMIX) channel. Two water streams enter the channel at the right and mix along its 800mm length. A laser induced fluorescence (LIF) image is included in the schematic to highlight the mixing layer.

Before optical flow analysis, the raw PIV images are pre-processed with the intensity normalization algorithm detailed in Kapulla et al., 2011. This step reduces laser light artifacts, and compensates for light sheet non-uniformities. Experimental images before and after processing are shown in Figure 11.

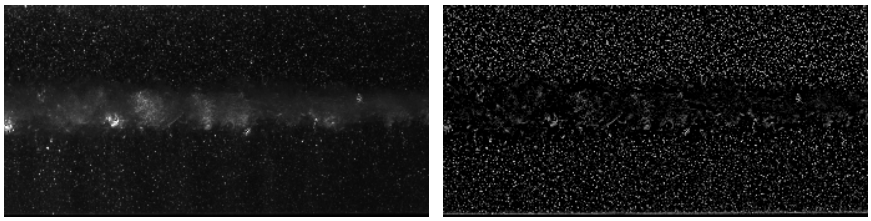

Figure 11: Experimental GEMIX image before (left) and after filtering (right).

After filtering, the no-slip boundary condition pattern is added to the top and bottom of the images to mimic the presence of the channel wall. A suitable smoothing parameter, α is determined using the previously proposed framework, with the resulting warp RMS curve shown in Figure 12.

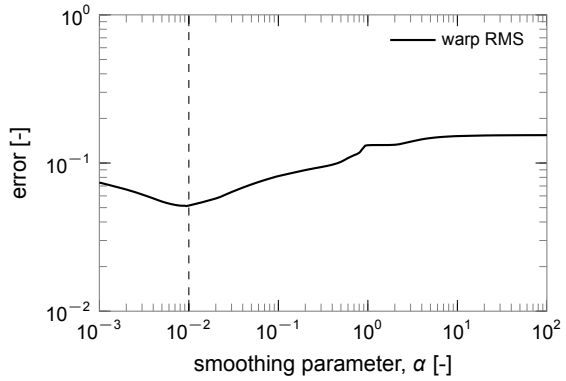

Figure 12: Warp RMS curve for a single GEMIX image pair.

A value of 0.01 is chosen for the smoothing parameter, and the remaining image pairs processed using 5 pyramid levels and 6 scale levels. The velocity averaged over all 1024 frames, along with velocity RMS values are shown in Figures 13 to 16.

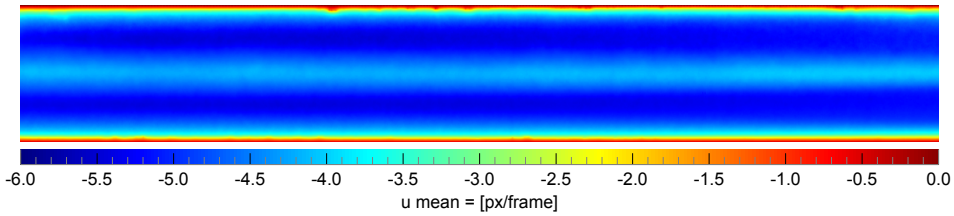

Figure 13: Mean u velocity field for series averaged experimental GEMIX images.

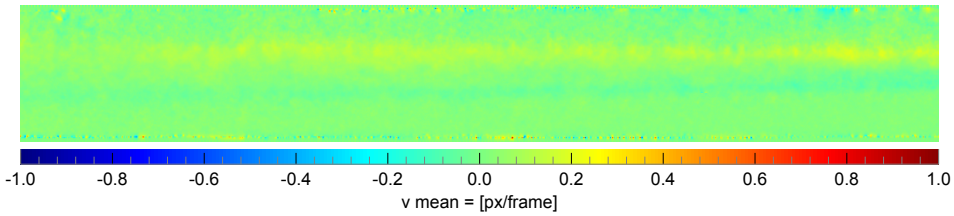

Figure 14: Mean v velocity field for series averaged experimental GEMIX images.

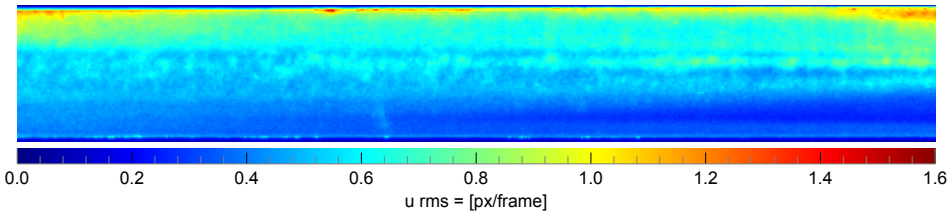

Figure 15: u RMS for the experimental GEMIX image series.

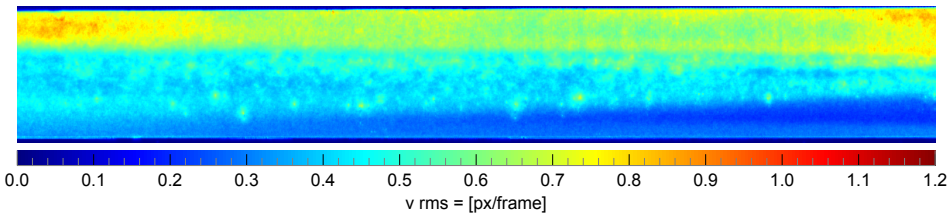

Figure 16: v RMS for the experimental GEMIX image series.

As expected from the use of no-slip boundary conditions, the average u and v velocities near the upper and lower channel walls is nearly zero, as seen in Figures 13 and 14. The fidelity of the

boundary layer is especially impressive considering the small number of pixels it is spread over – the vertical resolution of the PIV images, and thus the calculated velocity field, is 196 pixels.

In the velocity RMS plots (Figures 15 and 16), even though there is some noise caused by the reflection of laser light, the mixing region can be clearly seen, with the spreading of the mixing interface especially visible in Figure 16. To reduce the noise in the RMS plots would require a larger image set, or a higher smoothing value than calculated. Overall, the fidelity of the results are very good given the quality of the input images, and provide an excellent starting point for further investigation of density mixing experiments.

Conclusion

Methods for selecting the smoothing parameter and applying boundary conditions for analyzing PIV images have been presented. Application of the smoothing parameter selection framework has been demonstrated using a series of synthetically generated PIV images of poiseuille flow. The calculated velocity field using the selected smoothing parameter results in magnitude and endpoint errors less than 1% of the magnitude of the mean flow. The addition of no-slip boundary conditions to the input images has also been tested with a synthetic poiseuille image pair, along with synthetically images generated from an LES simulation of density mixing as reported in Kapulla et al., 2011. In both cases, the velocity profile near the wall is more faithfully reproduced when using data-driven boundary conditions. Finally, experimental PIV images are analyzed using the smoothing parameter selection framework along with no-slip boundary conditions. The resulting flow fields are of exceptionally high quality, and showcases the advantage of using optical flow in analyzing images with large amounts of blurring.

References

Atcheson, B., Heidrich, W., & Ihrke, I. (2009). An evaluation of optical flow algorithms for background oriented schlieren imaging. *Experiments in Fluids*, *46*(3), 467–476.

Baker, S., Scharstein, D., Lewis, J., Roth, S., Black, M., & Szeliski, R. (2011). A database and evaluation methodology for optical flow. *International Journal of Computer Vision*, *92*(1), 1–31.

Carlier, J. (2005). *Second set of fluid mechanics image sequences.* European Project 'Fluid image analysis and description' (FLUID).

Eggertson, E., Kapulla, R., Fokken, J., & Prasser, H.-M. (2011). Turbulent mixing and its effects on thermal fatigue in nuclear reactors. *World Academy of Science, Engineering and Technology*, *52*(1), 206–213.

Horn, B. K., & Schunck, B. G. (1981). Determining optical flow. *Artificial Intelligence*, *17*(1), 185 – 203.

Kapulla, R., Hoang, P., Szijarto, R., & Fokken, J. (2011). Parameter sensitivity of optical flow applied to PIV images. In *Proceedings of the Lasermethoden in der Strömungsmeßtechnik.* Ilmenau.

Krajsek, K., & Mester, R. (2007). Bayesian model selection for optical flow estimation. In *Proceedings of the Conference on Pattern Recognition* (Vol. 4713, pp. 142–151). Springer Berlin Heidelberg.

Ng, L., & Solo, V. (1997). A data-driven method for choosing smoothing parameters in optical flow problems. In *Proceedings of the International Conference on Image Processing* (Vol. 3, pp. 360–363).

Quénot, G. M., Pakleza, J., & Kowalewski, T. A. (1998). Particle image velocimetry with optical flow. *Experiments in Fluids*, *25*(3), 177–189.

Ruhnau, P. (2006). *Variational fluid motion estimation with physical priors*. Unpublished doctoral dissertation, Universität Mannheim.

Ruhnau, P., Kohlberger, T., Schnörr, C., & Nobach, H. (2005). Variational optical flow estimation for particle image velocimetry. *Experiments in Fluids*, *38*(1), 21–32.

Tu, Z., Xie, W., Hürst, W., Xiong, S., & Qin, Q. (2012). Weighted root mean square approach to select the optimal smoothness parameter of the variational optical flow algorithms. *Optical Engineering*, *51*(3), 037202-1–037202-9.

Zimmer, H., Bruhn, A., & Weickert, J. (2011). Optic flow in harmony. *International Journal of Computer Vision*, *93*(3), 368–388.